AIAA Propulsion and Energy Forum
August 9-11, 2021, VIRTUAL EVENT
AIAA Propulsion and Energy 2021 Forum

10.2514/6.2021-3384

Performance Measurements of a 5 kW-Class Rotating Magnetic Field Thruster

Christopher L. Sercel*, Joshua M. Woods †, Tate M. Gill ‡, and Benjamin A. Jorns§
University of Michigan, Ann Arbor, MI, 48109

The performance of a rotating magnetic field (RMF) thruster is experimentally investigated. A 5 kW-class test article is designed and constructed based on derived scaling laws, and the operation is characterized at an average power varying from 3-4.5 kW, with pulse widths of 200 μs, and duty cycle of 1.5%. High speed video is employed to qualitatively investigate plasma shot behavior, antenna current traces are recorded to measure the energy which is coupled into the plasma during each shot, and direct, time-averaged thrust data is taken using an inverted pendulum thrust stand operated in displacement mode. Coupling efficiency is shown to reach values of over 50%, but total per-shot efficiency remains below 1%. Parametric studies show trends such as thrust, efficiency, and specific impulse all scaling with specific energy, which matches with behavior of similar pulsed plasma thrusters and suggests a potential strategy for an improved design.

Nomenclature

α	Plasma ionization fraction
Δt	Pulse duration
δ	Classical resistive skin depth
$\dot{m}$	Propellant mass flow rate
η	(No subscript) Plasma resistivity
η_c	Coupling efficiency
η_T	Total thruster efficiency
η_{pl}	Plume Efficiency
$\langle c \rangle$	Propellant neutral thermal speed
μ_0	Permeability of free space
ν_{ei}	Electron-ion collision frequency
ω	Rotating magnetic field frequency
ω_{ce}	Electron cyclotron frequency
$\vec{B_{ind}}$	Magnetic field induced by driven plasma currents
$\vec{B_{RMF}}$	Rotating magnetic field
$\vec{E}$	Electric field
$\vec{g}$	Total current to current density local scaling factor
$\vec{j}$	Current density
$\vec{v}_e$	Electron velocity
e	Electron charge
F	Force
f	Pulse repetition rate
I	Current
$I_{DC,p}$	Current drawn from the DC supply during a plasma-loaded shot
$I_{DC,v}$	Current drawn from the DC supply during a vacuum shot
$I_{x,p}$	Antenna current trace through the X antenna during a plasma-loaded shot
$I_{x,v}$	Antenna current trace through the X antenna during a vacuum shot
$I_{y,p}$	Antenna current trace through the Y antenna during a plasma-loaded shot

*PhD Candidate, Department of Aerospace Engineering, AIAA Student Member
†PhD Candidate , Department of Aerospace Engineering, AIAA Student Member
‡PhD Candidate , Department of Aerospace Engineering, AIAA Student Member
§Assistant Professor, Department of Aerospace Engineering, AIAA Associate Fellow

$I_{y,v}$	Antenna current trace through the Y antenna during a vacuum shot
l	Thruster length
L_p	Plasma effective inductance
M	Atomic mass of propellant
m^*	Mass ejected per-pulse
m_e	Electron mass
N	Total particles per pulse due to steady-state thermal diffusion
n_e	Electron density
p^*	Impulse per-pulse
R_p	Outer radius of plasma
$R_{LC,x}$	Effective resistance of the X antenna resonator
$R_{LC,y}$	Effective resistance of the Y antenna resonator
T	Thrust
U^*	Energy per-pulse
u_e^*	Effective exhaust velocity per-pulse
U_p	Energy added to the plasma per-pulse
$U_{DC,p}$	Energy sourced from the DC supply during a plasma-loaded shot
$U_{DC,v}$	Energy sourced from the DC supply during a vacuum shot
$U_{LC,p}$	Energy added to the LC resonator in a plasma-loaded shot
$U_{LC,v}$	Energy added to the LC resonator during a vacuum shot
U_{pulse}	Energy supplied by the PPU in a single pulse
$U_{R,v}$	Energy lost to the charging resistor during a vacuum shot
U_{spinup}	Energy required to drive electrons into synchronous rotation with the RMF
$V_{BB,p}$	Voltage measured accross the backing capacitor bank during a plasma-loaded shot
$V_{BB,v}$	Voltage measured accross the backing capacitor bank during a vacuum shot
$V_{DC,p}$	Voltage on the DC supply during a plasma-loaded shot

I. Introduction

The rotating magnetic field (RMF) thruster is a potentially enabling type of inductively coupled, pulsed plasma thruster (IPPT). As a class of electric propulsion device, IPPTs employ time-dependent currents and electric fields to induce currents in their propellant, thereby leading to Lorentz forces that accelerate the exhaust to high speed. This acceleration mechanism has a number of potential advantages compared to more conventional, steady-state electric thrusters. Perhaps foremost of these is a comparatively high achievable specific power, which owes to the tendency for these and similar devices' thrust to scale quadratically with the input current rather than linearly, as is the case for most conventional propulsion techniques [1]. Its pulsed nature also makes the IPPT highly throttleable [2], as the duty cycle can be adjusted independently to any pulse-specific operational parameters. Finally, since no plasma-wetted electrodes are necessary to operation, this class of thrusters is potentially compatible with non-inert propellants such as water and carbon dioxide, both important resources which can be found in-situ [3]. This is important as NASA looks toward investigating in-situ resource utilization (ISRU) on the moon as part of the Artemis project [4].

While IPPTs have been the subject of extensive investigation due to their potential advantages, there are a number of technical challenges that have inhibited their transition to operational use. Foremost among these challenges is power-processing unit (PPU) lifetime concerns. Because IPPTs rely on pulses of high voltage and current, longevity of power switches becomes a limiting factor. While any switching element has some risk of failure due to cycling wear, the strong transients that must be driven in an IPPT exacerbate this problem. The RMF thruster has the potential to avoid this major pitfall due to its unique principle of operation. The RMF thruster functions by inducing a strong azimuthal current in a cylindrical plasma by entraining electrons in a rotating magnetic field. Under so-called "penetration" conditions, the induced current depends on the RMF rotational frequency rather than magnitude [5]. Therefore the switched transients necessary to run the thruster can be significantly lower than more conventional IPPT devices, leading to better lifetime of power-switching elements.

Because the RMF thruster is promising in principle, several efforts have been made to progress the state of the art. Much early research was done by MSNW LLC on their Electrodeless Lorentz Force (ELF) [6] thruster. Performance data was taken on the ELF thruster using a ballistic pendulum to measure the impulse from a shot to make efficiency measurements [7], and research was conducted as to the ISRU-applicability of the device as well [8]. In more recent years, Furukawa *et al.* have developed a test unit with electrical and plasma-based measurements [9], as well as ballistic pendulum-type impulse measurements [10]. Furukawa has also performed measurements of azimuthal current by directly measuring magnetic field gradients using Hall effect probes to verify the current drive mechanism [11]. Even more recently, Sun *et al.* have developed their proof-of-concept RMF-driven thruster for further research [12].

Despite these past and current efforts, there is some ambiguity about the fidelity of performance measurements reported to date. For example, all published performance measurements we are aware of have been indirect, either making use of measured plasma parameters or ballistic pendulums to measure impulse per shot. These indirect approaches can be problematic. In the case of estimating performance with plasma parameters, a performance model must necessarily be assumed, but there exist no conclusively verified performance models for RMF thrusters at this point. Ballistic pendulums, meanwhile, can exhibit difficulties in calibration and implementation which yield their results unreliable relative to more standard thrust stand measurements. In both measurements techniques—ballistic pendulum and plasma parameter-based—the data largely have typically been shot-by-shot rather than steady state, obscuring whether the device truly generates net thrust.

The fidelity of the test environment from past studies also invites questions about the accuracy of previous performance measurements. Most published measurements to date have been performed in non-space-like conditions. The thrusters were mounted to the side of the vacuum facility with the thruster body effectively forming part of the chamber wall, then fired into the chamber. In the case of the ELF thruster, shots also were fired directly into a facility-based confining magnetic field, which could potentially remove factors such as the natural divergence of the plume or even cause anomalously high impulse per shot by providing an additional magnetic field with which plasma currents can interact.

Thus, although much valuable work has been done to investigate the physics of the RMF thruster, it is not clear if and what the actual baseline performance is. Before refinement can be done in earnest, the need is apparent for definitive performance measurements so that models of thruster operation can be better verified or dismissed as the case may be.

The goal of this work is to address this gap by providing direct performance measurements of an RMF-FRC device over a wide range of operating conditions. We organize the paper in the following way. In Section II, we discuss the major principles underpinning the RMF thruster concept. In Section III, we discuss the thruster design and test setpoint selection. In Section IV, we detail the experimental setup used in collection of the data, including thruster design, power-processing unit design, thrust stand measurement procedures, and current waveform measurement procedures. Section V details the analysis techniques used to extract useful information from the data taken. In Section VI, we present the experimental data, including plasmoid images, antenna current waveforms, and performance metrics. In Section VII, we discuss the physical implications of these results, and address paths forward for improving thruster performance. Finally, we summarize this work and conclude in Section VIII.

II. Principles of Operation

In this section, we briefly review the principles of operation of the RMF thruster, highlighting key physical processes. We first discuss the mechanism for current induction and thrust generation, then touch on key challenges for efficient operation. We then discuss how these principles are applied to the design of the PEPL RMFv2, the test unit used in this study.

A. Inducing Current with RMF

Figure 1 shows the canonical geometry of the RMF thruster. It consists of a seed plasma source which flows into a plasma-bounding cone. The cone is surrounded by a pair of saddle coils, clocked 90 degrees relative to each other, as well as large steady-state electromagnets. When current flows through a saddle coil, it effectively forms a Helmholtz pair oriented in either the X or Y direction and therefore generates a corresponding unidirectional magnetic field. Sending a sinusoidal current through the coil, the magnetic field's direction and magnitude oscillates. The RMF is generated when current through each coil oscillates 90 degrees out of phase. The bias field, meanwhile, is generated by the electromagnets, and current through each magnet is chosen such that the field is tangent to the plasma-bounding cone along its walls.

As shown in Figure 2, the current drive mechanism can be illustrated in the simplest case by considering the rotating magnetic field given by

$$\vec{B}_{RMF} = |B_{RMF}| \left(\cos(\omega t)\hat{x} + \sin(\omega t)\hat{y}\right), \tag{1}$$

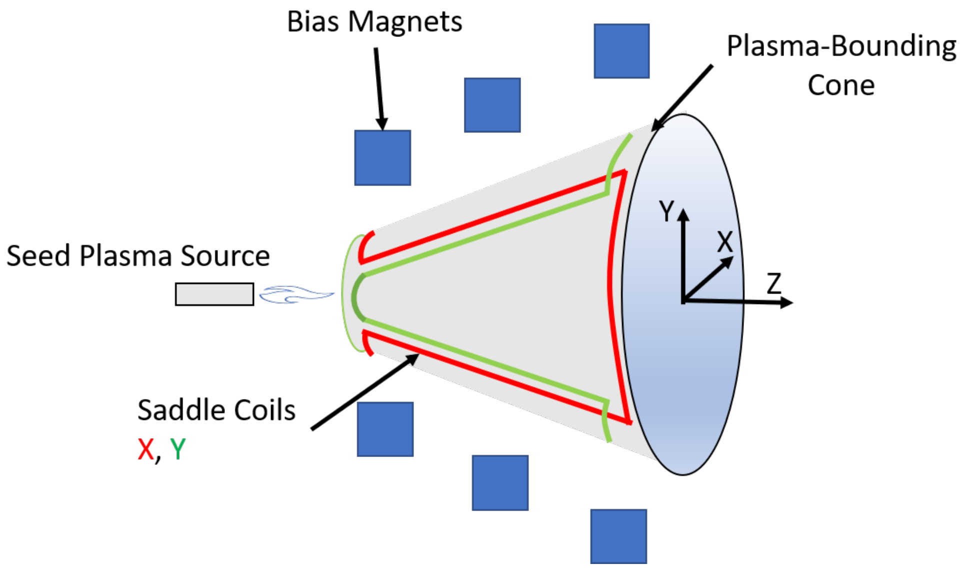

Fig. 1 Canonical geometry of an RMF thruster

where ω is the RMF frequency, and where coordinate convention is as shown in Figure 1. This in turn will necessarily induce an electric field described by Faraday's Law:

$$\vec{E} = \omega \left| B_{RMF} \right| \left(x \cos(\omega t) + y \sin(\omega t) \right) \hat{z}. \tag{2}$$

Assuming non-inertial, collisionless electrons and cold ions, Ohm's law states

$$\vec{E} = -\vec{v}_e \times \vec{B}, \tag{3}$$

for electron velocity $\vec{v}_e$. Substituting Equations 1 and 2 into Ohm's law, we find that the electron velocity must be given by

$$\vec{v}_e = \omega \left(-y\hat{x} + x\hat{y} \right) = \omega r \hat{\theta} \tag{4}$$

so that current density is given by

$$\vec{j} = -e n_e \omega r \hat{\theta}. \tag{5}$$

B. Thrust Generation

Once the azimuthal current is induced, it interacts with the radial component of the magnetic field via the Lorentz force as shown in Figure 3 to produce a body force on the plasma, given by

$$F = \iiint B_r j_\theta d^3 r, \tag{6}$$

where B_r is the radial component of the magnetic field and j_θ is the induced azimuthal current density. Due to the conical geometry, B_r will have a contribution both from the applied bias field and from the self-field generated by the plasma such that $\vec{B} = \vec{B}_{ind} + \vec{B}_0$. The Biot-Savart Law gives the induced magnetic field as

$$\vec{B}_{ind} = \frac{\mu_0}{4\pi} \iiint \frac{\vec{j}(\vec{r}') \times \vec{r}'}{r'^3} d^3 r', \tag{7}$$

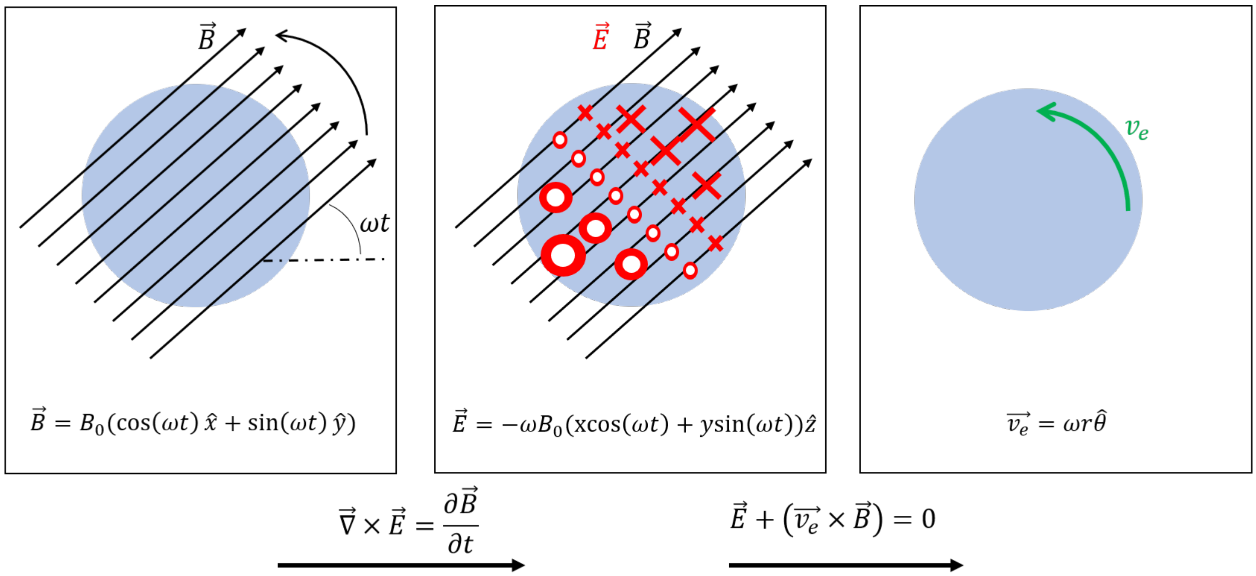

Fig. 2 Azimuthal current drive mechanism used in the RMF thruster

where r' is a dummy variable integrated over all space. If we define a new variable $\vec{g}$ such that $\vec{g}I_\theta \equiv \vec{j}$, where I_θ is the total azimuthal current, Equation 6 becomes

$$F = \iiint \left(I_\theta g_\theta B_{0r} + \frac{\mu_0}{4\pi} I_\theta^2 g_\theta \iiint \frac{\vec{g}(\vec{r}') \times \vec{r}'}{r'^3} \right) d^3 r'. \tag{8}$$

Equation 8 can be integrated again in time to arrive at the total impulse of a given plasma shot. Equation 8 provides two key takeaways. First, there exist both linear and quadratic scaling terms for the dependence of current on force. The quadratic scaling term is critical to the very high specific powers achievable to all IPPTs and is why these thrusters lend themselves towards pulsed operation. Second, per our analysis from the previous section, the impulse generated by a plasma shot depends on the RMF frequency, not magnitude. The thruster can therefore be allowed to pulse much lower current and voltage transients relative to other inductively-driven pulsed thrusters, which could allow for improved lifetime of circuit components.

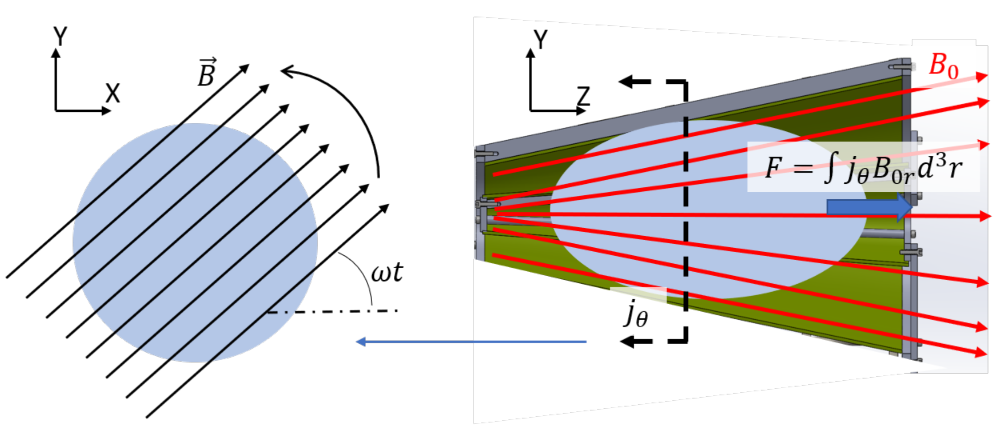

Fig. 3 The rotating magnetic field drives an azimuthal current in the plasma, which interacts via the Lorentz force with the radial component of the magnetic field to produce thrust.

C. Scaling Laws for Design

1. RMF Penetration

A chief design consideration is the concept of RMF penetration, a concept explored by Jones and Hugrass [13]. In the above explanation for the current drive mechanism, non-ideal effects such as collisional resistivity and AC skin depth are neglected for the sake of simplicity. In reality, these effects impact the behavior of the current which can be driven in the plasma. The penetration condition can be determined by comparing a few key parameters:

$$\left(\frac{\nu_{ei}}{\omega_{ce}}\right)^2 \left(\frac{R}{\delta}\right)^2 << 1, \tag{9}$$

where ν_{ei} is the electron-ion collision frequency, ω_{ce} is the electron cyclotron frequency about the RMF, δ is the classical AC skin depth, and R is the total radius of the plasma. Physically, this expression can be broken into two intuitive requirements. The first, depending on the ratio of collision to cyclotron frequency, enforces that the electrons are sufficiently tied to field lines to be considered entrained. The second, depending on the ratio of classical skin depth to plasma radius, means the field will not be screened out by eddy currents. This condition can be used to ensure that a device has sufficient RMF magnitude to achieve penetration by the addition of thruster-specific information.

First, we address the electron cyclotron frequency term, given by

$$\omega_{ce} = \frac{eB_{RMF}}{m_e}. \tag{10}$$

We assume the RMF is generated by a 2-phase antenna consisting of two Helmholtz pairs. The magnitude of the magnetic field generated by a Helmholtz pair near the center of the loops is a well-known result, given by

$$B_{RMF}(z) = \left(\frac{4}{5}\right)^{\frac{2}{3}} \frac{\mu_0 I_{RMF}}{R_{antenna}(z)} = \sqrt{3}\left(\frac{4}{5}\right)^{\frac{2}{3}} \frac{\mu_0 I_{RMF}}{R(z)}, \tag{11}$$

where $R_{antenna}$ is the radius of each loop forming the pair, and due to the geometry of the thruster, the antenna loops are roughly a factor of $\sqrt{3}$ smaller than the radius of the cone structure. If this is the case, the electron cyclotron frequency can be written

$$\omega_{ce} = \sqrt{3}\left(\frac{4}{5}\right)^{\frac{2}{3}} \frac{e\mu_0 I_{RMF}}{m_e R(z)}. \tag{12}$$

Next we address the collision term. We recognize that collisions serving to reduce electron field line entrainment will come from neutrals as well as ions since we will not necessarily have a fully-ionized plasma at all times. Thus we use $\nu = \nu_{ei} + \nu_{en}$ in Equation 9, with ν_{en} being electron-neutral collisions. Therefore we have

$$\left(\frac{\nu_{ei} + \nu_{en}}{\omega_{ce}}\right)^2 \left(\frac{R}{\delta}\right)^2 << 1. \tag{13}$$

We turn to Goebel and Katz (2008) [14] for the values for ν_{ei} and ν_{en}, given for Xenon as

$$\nu_{ei} = \left(2.9 \times 10^{-12}\right) \frac{n_e \ln \Lambda}{T_{eV}^{\frac{3}{2}}} \tag{14}$$

$$\nu_{en} = 6.6 \times 10^{-19} \left[\frac{.25T_{eV} - 1}{1 + (.25T_{eV})^{1.6}}\right] n_n \sqrt{\frac{8kT_e}{\pi m_e}} \tag{15}$$

in which $\ln \Lambda$ is the so-called "coulomb logarithm," T_{eV} is the electron temperature in eV, and n_n is the neutral density.

Third, we address the skin-depth term. Classical AC skin depth is given by

$$\delta = \sqrt{\frac{2\eta}{\mu_0 \omega}}, \tag{16}$$

with η being the resistivity of the conductive medium. Resistivity can be put in terms of collision frequency using

$$\eta = \frac{m_e \nu}{e^2 n_e}, \tag{17}$$

which gives us

$$\delta = \sqrt{\frac{2m_e\left(\nu_{ei} + \nu_{en}\right)}{\mu_0 e^2 n_e \omega}}. \tag{18}$$

To determine the densities needed by Equations 14, 15, and 18, we further assume a radially-uniform density profile whose axial distribution is dictated by thermal diffusion so that the density is given by

$$n_e(z) = n_0 \alpha \frac{R^2(z)}{R_0^2} \tag{19}$$

$$n_n(z) = n_0 \left(1 - \alpha\right) \frac{R^2(z)}{R_0^2} \tag{20}$$

where $n_e(z)$ is the electron density at any given axial location in the cone, n_0 is the total density at the cone's throat, α is the ionization fraction of the plasma, R_0 is the radius at the cone's throat, and $R(z)$ is the cone's radius at the given axial location.

We now substitute Equations 19 and 20 into Equations 14, 15, and 18 for final expressions for ν_{ei}, ν_{en}, and δ. These are then substituted into Equation 13. After simplification and evaluation of constants, we find the expression

$$\dot{m} << \left(2.0 \times 10^8 \left(\frac{1}{\alpha} - 1\right) + 1.7 \times 10^9\right)^{-\frac{1}{2}} \frac{I_{RMF}}{\alpha\sqrt{\omega}}, \tag{21}$$

where we note that the radius of the cone has cancelled out, yielding a single relation valid for the entire cone. This relation gives a limit to the allowable mass flow rate of Xenon into a cone-shaped RMF thruster with Helmholtz-pair-style antennas to ensure penetration given an anticipated degree of ionization in the seed plasma. Equation 21 tells us that if the plasma is too dense, either eddy currents will screen out the field at the edge of the plasma, or collisions will prevent electron entrainment despite apparent penetration. For a worst case, $\alpha = 1$ can be taken, corresponding with an assumption of full ionization. Meanwhile, in the case of no ionization—$\alpha = 0$—mass flow can take any value since there is no conductive medium to screen out the RMF.

2. *Per-Pulse Energy Target*

While Equation 21 gives information about the propellant flow given PPU limitations, some sense for thruster size is also necessary to design a test unit. To find a scaling law for roughly how large the thruster should be, we consider the plasma as an inductor. As such, the plasma will have some capacity to store energy owing to the driven azimuthal current. We require that the energy per pulse available from the PPU be commensurate to the energy required to drive the azimuthal current in the plasma. The condition we seek to match becomes

$$U_{pulse} = 2\eta_c U_{spinup} \tag{22}$$

where U_{pulse} is the available energy from the PPU per pulse, η_c is the coupling efficiency which describes the fraction of energy transferred from the antennas to the plasma, and U_{spinup} is the inductive energy associated with the azimuthal current in the plasma for full electron entrainment by the RMF. We have added an additional arbitrary factor of 2 to our required energy per pulse because actual acceleration mechanisms are not clear; in the event that energy coupling to the plasma does not take the shape of a clean delta function, energy might continue to couple to the plasma throughout the acceleration process, thus allowing the addition of more than U_{spinup} to the plasma.

Because we consider the plasma as an inductor in this rough analysis, we take

$$U_{spinup} = \frac{1}{2} L_p I_\theta^2 \tag{23}$$

where L_p is the effective self-inductance of the plasma. For the sake of an order of magnitude estimate, we consider the plasma's self inductance to take the form of a single-turn solenoid of length l and radius R, where l and R_{avg} are the thruster's length and average radius, respectively. In this case,

$$L_p = \frac{\mu_0 \pi R_{avg}^2}{l}. \tag{24}$$

Next, we estimate the azimuthal current by considering the total number of electrons present in the cone before a pulse. Because of the relatively low duty cycle we operate the thruster at, neutral particles entering the cone have sufficient time to reach steady-state density between pulses. For reference, the characteristic fill time of neutrals throughout our thruster is approximately 1.3 ms, while the time between pulses is approximately 13 ms, which is limited by the PPU (see Section III). Therefore, we assume thermal diffusive steady-state at the beginning of each pulse. In other words, the mass flux through the exit plane of the cone must equal the mass flow into the cone. Mass flux through a surface is given by

$$\dot{m} = \frac{1}{4} n A M \langle c \rangle \tag{25}$$

where n is the density, $A = \pi R^2$ is the area, M is atomic mass, and $\langle c \rangle$ is thermal speed, given by $\langle c \rangle = \sqrt{\frac{8kT}{\pi M}}$. The density is therefore given by

$$n = \frac{\dot{m}}{4\pi R^2 M \langle c \rangle}. \tag{26}$$

This density can be integrated throughout the volume of a cone of length l to yield the expression for the total number of particles in the cone before ringing the RMF:

$$N = \frac{4\dot{m} l}{M \langle c \rangle}, \tag{27}$$

where the cone angle has dropped out, yielding an expression dependent only on the final length (or alternatively, radius) of the cone. If each particle is ionized by the RMF and each electron is entrained, rotating at a frequency ω, the azimuthal current will be given by

$$I_\theta = eN\omega = \frac{4e\omega \dot{m} l}{M \langle c \rangle}. \tag{28}$$

Plugging back into Equation 23, we have

$$U_{spinup} = \frac{16 \mu_0^2 R_{avg}^2 l \dot{m}^2 \omega^2}{\langle c \rangle^2 M^2}, \tag{29}$$

which can be compared to the available energy per pulse with Equation 22 to relate the thruster geometry to the PPU capabilities.

D. Role of flux conservers

Flux conservers are conductive bands that surround the tube or cone containing the plasma and RMF antennas. These features in principle can improve the confinement capability of the device by preventing lines of magnetic flux from escaping the plasma tube, at least on short time scales. This serves to increase the radial magnetic pressure on the plasmoid to bring about a denser plasma via radial pressure balance between thermal and magnetic pressures. In fact, the lossiness of the flux conservers used in an FRC plasma containment device, the inspiration for the RMF thruster from the fusion community, is often considered an important figure of merit applications [15]. As a carry-over from the fusion beginnings of the RMF thruster, flux conservers are often included in the designs with the argument that the increased radial magnetic pressure will help accelerate the plasma, not unlike how toothpaste is squeezed from a tube. However, it can be shown by considering a circuit model that if the goal is axial acceleration via the Lorentz force, flux conservers, and indeed any conductive elements surrounding the plasma, will serve to reduce the overall efficiency of the device [16]. This is the case even when taking the flux conservers to be completely lossless, as inductive energy is invariably left behind when currents are induced in the flux conservers by the change in current of the plasmoid as it is accelerated. Therefore to achieve efficient acceleration, we should minimize the amount of conductive structure near to the plasma and RMF antennas.

III. RMF Thruster Design

As the goal in our work is to establish the baseline operation of an RMF thruster, we first want to design a system that we have the highest confidence will produce measurable thrust and performance. To this end, we have applied the principles outlined in Section II, as well as insights from our previous work [17] to design a new test article. We describe the key components in the following section, concluding by relating the design back to known scaling laws.

A. Thruster body

As shown in Figure 4, the main body of the thruster, named the PEPL RMFv2, forms a truncated cone with a 14° half-angle. The opening at the downstream end measures approximately 8" in diameter, with an upstream (throat) opening of 3". This structure is lined with sheet mica to prevent the outward expansion of gas or plasma and built so that the RMF antennas can mount directly to it to minimize the distance from the antennas to the plasma itself for greatest coupling. The main structure and the magnet bobbins are made from a scaffold of G10 and FR4 pieces rather than machined from metal, which serves to produce a very lightweight, inexpensive test device in addition to the primary effect of minimizing structural mutual inductance (see previous section).

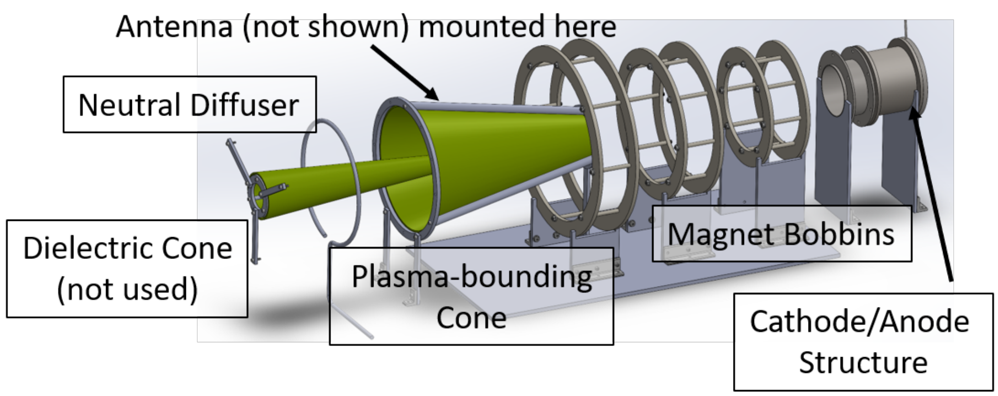

Fig. 4 Exploded view of the PEPL RMFv2. Construction from G10 scaffold, with plasma-bounding surfaces made of mica sheets. Optional dielectric cone (not used in this study) can be mounted inside the mouth to convert the solid to an annular cone to alter flow properties.

B. Bias Magnetic Field

The bias magnetic field is generated by three electromagnets situated about the body of the thruster. To find the desired current setpoints for each magnet, the magnetic fields resulting from a nominal current through each was

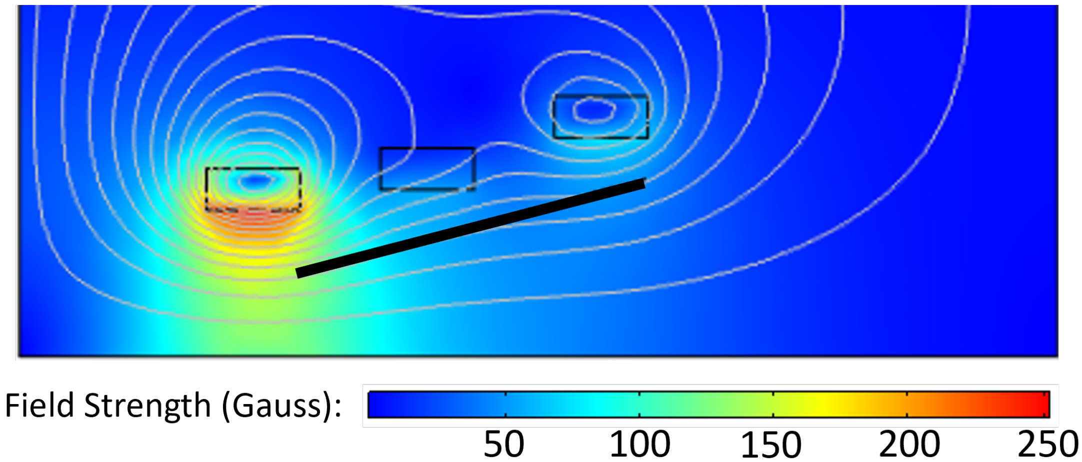

Fig. 5 Map of bias field at 120 G centerline peak strength condition. Boxes indicate magnet locations. Solid line indicates thruster wall position.

measured using a Hall effect probe. The fields were then superposed and scaled to produce a field shape which is tangent to the cone at its edge, as shown in Figure 5. There do not yet exist comprehensive scaling laws which take into account bias field shape. This tangent field line condition was chosen from the perspective of electron movement. It represents a middle ground between a too-strongly divergent magnetic field in which electrons tied to field lines would be forced into the walls, and a too weakly divergent field in which electrons remain on centerline where they will not contribute to the overall force on the plasma. This field shape has the effect of a rapidly diminishing field strength away from the throat of the thruster, a necessary side effect of the geometry.

Two settings were chosen: one at approximately 80 G centerline maximum strength, and one at 120 G. Field strengths were chosen so that, under conditions of full entrainment, the induced magnetic field at centerline would be approximately twice the bias field, forming a Field-Reversed Configuration (FRC) under ideal circumstances. While the FRC is not considered important to this particular study, it allows easier comparison to other RMF thrusters such as the ELF [7] which do claim field reversal.

C. RMF antenna

Each RMF antenna is bent in the form of a saddle coil, with each loop on an opposite side of the cone. The antennas are bent such that each loop subtends an approximately 60° portion of the cone's cross section. The antennas themselves are formed from copper tubing to minimize their circuit resistance given skin depth considerations and allow for water cooling during operation.The two antennas are clocked 90° relative to each other so that, when fed oscillating currents which are offset 90°, a rotating magnetic field of relatively uniform magnitude is formed. An example field map of the RMF, measured at approximately 10 cm downstream of the cone's throat and scaled to reflect a peak current of 2 kA, is shown in Figure 6. We measured this by running DC current through each antenna individually, then generating a map using Hall effect probe measurements. The resulting fields were then superposed on each other to verify rotation.

D. Pre-ionizer

A pre-ionization source is a necessary component to the operation of the RMF thruster. This provides the seed plasma necessary for facilitating the RMF spin up. For this design, we used a LaB_6 hollow cathode operating with Xenon as the propellant. We note that in a more mature device, an ionization scheme would be chosen which does not require a noble gas so that the thruster can be tested on ISRU propellant options. However, lab design heritage and expertise made the choice of hollow cathode easiest to work with, and our research interest is in the acceleration mechanism rather than the design of an inductive pre-ionizer. The cathode is able to form a discharge of 20 A to the steel anode structure immediately surrounding it and operates with 15 sccm Xe of flow. For flow conditions requiring more than 15 sccm, a secondary neutral injection tube was used.

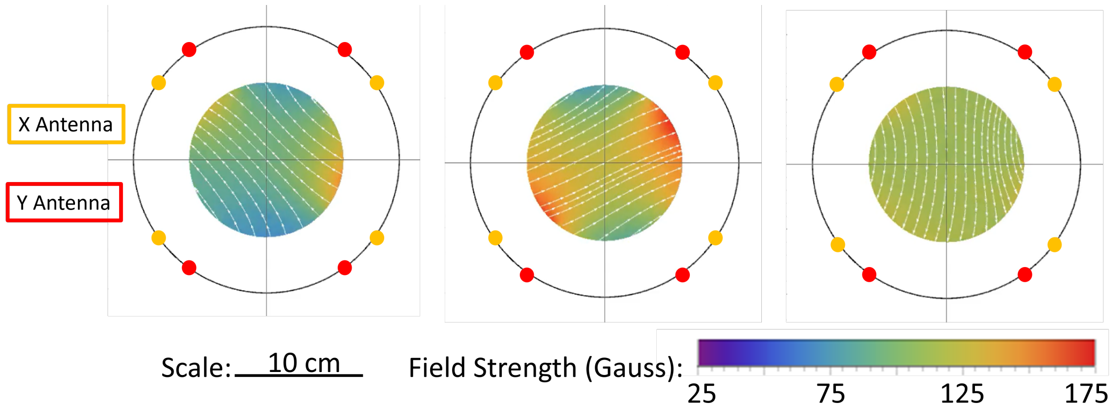

Fig. 6 Map of RMF measured approximately 10 cm downstream of the cone's throat at three instants throughout a cycle to illustrate rotation. Maps correspond to peak antenna currents of 2 kA.

E. Gas injection

The neutral injection tube, which can be seen around the rim of the thruster mouth in Figure 9, is formed from two concentric steel tubes bent into a circle. Propellant flows from the inner tube to the outer through small holes to ensure even pressure throughout the body of the outer layer. Holes in the outer tube direct flow upstream toward the thruster's throat to maximize residence time of neutral gas inside the cone and attempt to direct gas toward the cone's outer walls, where the effect of the RMF will be felt most strongly.

F. Power supply

To supply the necessary high current pulses to the RMF antennas, we collaborated with Eagle Harbor Technologies to develop a power-processing unit (PPU). Figure 7 shows a simplified circuit diagram of the PPU. Tuning capacitor banks were installed near the thruster in the vacuum chamber to create a series resonant LC circuit with the antenna as the inductor. This circuit is then pulsed at resonance using an H-bridge with dual-IGBT switches backed by a larger capacitor bank, which is in turn connected to a DC power supply. This setup has the advantage of generating current pulses whose amplitude is limited only by the real resistance of the circuit, though a tuning procedure must be carried out to ensure the pulses are sent at the resonant frequency. This supply is able to deliver approximately 5 kW of power combined to both antennas for a duration of 5 minutes to avoid any risk of overheating.

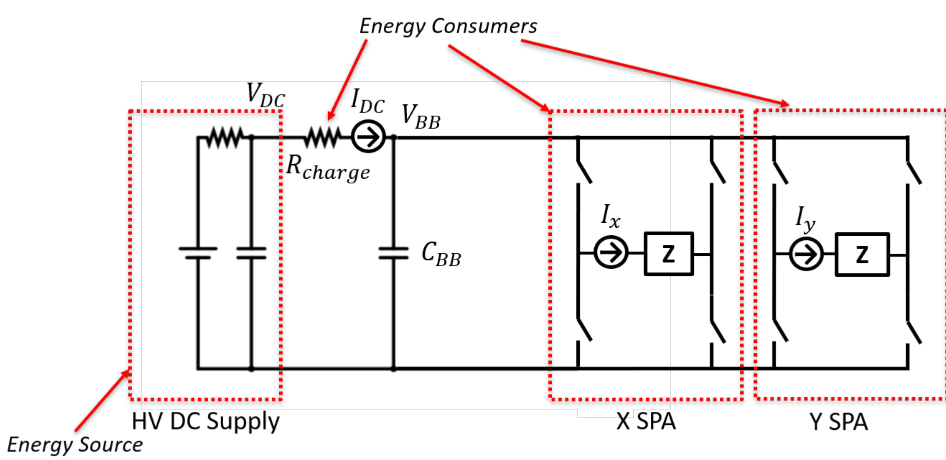

Fig. 7 Simplified circuit diagram of the PPU. A DC supply provides power to a large backing capacitor bank, which is used along with an H brige to send pulses of energy into LC tanks formed from each antenna and an accompanying tuning capacitor bank.

G. Relation of Thruster Design to Scaling Laws

The basic scaling laws for penetration and cone sizing outlined in Section II.C were used to determine the operating conditions and rough thruster size for the PEPL RMFv2. Because both conditions hinge on the performance of the PPU, we first determined what range of operation was physically reasonable with the Eagle Harbor system. To this end, the RMF PPU can supply pulses with up to 2 kA current amplitude at approximately 400 kHz RMF frequency. These pulses can draw up to approximately 25 J per antenna for a total of 50 J per shot, operating up to 75 Hz repetition rate.

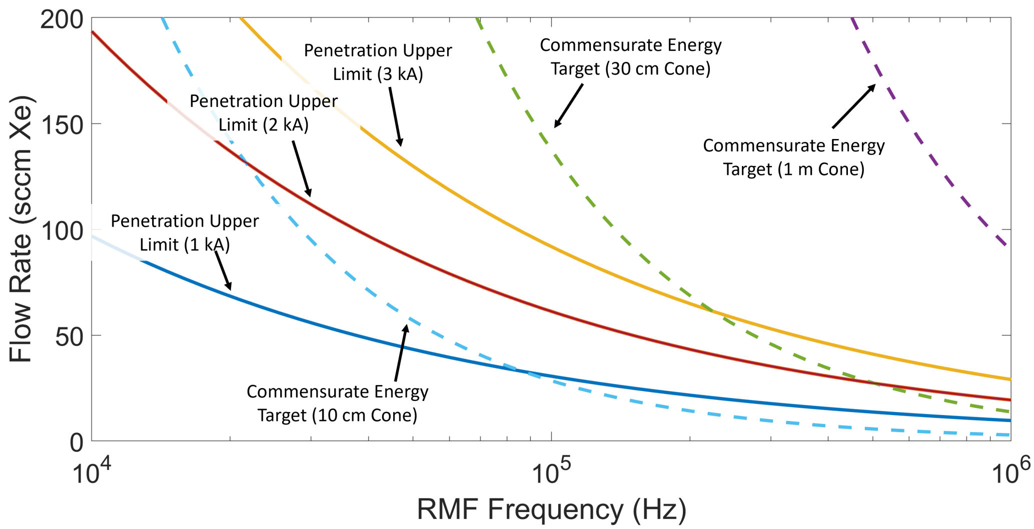

Fig. 8 Upper limits on propellant flow as a functions of RMF frequency as put forth by Equations 21 and 29.

Figure 8 illustrates the design conditions set out in Equations 21 and 29, which we used to determine the thruster's design. To ensure penetration, maximum propellant flow must remain below the penetration limit curve associated with the antenna current magnitude employed. To ensure commensurate energy between inductive capacity of the plasma and the PPU's output, the thruster should be operated along the energy target curve associated with its size. To produce Figure 8, a safety factor of 10 was applied to ensure the inequality in Equation 21, and Equation 29 was used with an anticipated coupling efficiency of 20% and a per-pulse energy of 50 J. Additionally, a cone half-angle was set to 14° to roughly match previous efforts.

Given the PPU's limitation of 2 kA and anticipated RMF frequency of 400 kHz, we selected a thruster length of 30 cm, as the associated energy limit curve intersects the 2 kA penetration limit curve at approximately 400 kHz. At this design condition we would then plan to operate using a maximum of approximately 50 sccm Xe propellant flow to ensure effective penetration and energy matching .

IV. Experimental Setup

The goal of this work is to characterize the steady-state performance of the test article outlined in the previous section. To this end, we describe in this section the test facility, operating points, and diagnostics.

A. Test facility

Testing was conducted at the University of Michigan in the Large Vacuum Test Facility (LVTF), a 6 m × 9 m vacuum chamber which employs cryogenic pumping surfaces mounted around its interior surface to achieve an effective Xenon pumping speed of up to 600,000 L/s [18]. A graphite beam dump was situated approximately 3 meters downstream of the thruster. A multitude of feedthroughs and ports allowed for observation of the thruster's behavior by both live and high speed video, along with necessary power to the cathode and RMF antennas. Diagnostics used to investigate device performance include antenna current waveform traces, high speed video, and thrust stand measurement. Antenna current waveforms were measured using a Pearson current monitor on each antenna line. High speed camera data was taken from the thruster's side with 50 kHz frame rate to ensure the evolution of the pulse could be seen.

B. Operating points

Keeping in mind the power limitations of the PPU and the thruster geometry, we operated the test article at a range of conditions, varying bias field magnitude (but not shape), propellant flow rate, and RMF magnitude. For all conditions, a repetition rate of 75 Hz with a pulse duration of 200 μs was chosen to maximize power to the thruster while avoiding thermal concerns in the PPU. We used bias fields of 80 G and 120G, flow rates of 15, 30, 45, and 60 sccm Xe, and peak antenna currents of 1.5, 1.7, and 1.95 kA. These flow rates were determined based on the penetration condition analysis presented in Section II. The bias field strengths were chosen to approximately equal the fields anticipated to be induced by the azimuthal current in the plasma. Antenna currents were chosen with the maximum setpoint limited by the PPU constraints. We also added a 200 sccm Xe, 120 G, 1.7 kA setpoint to briefly explore the very high flow regime as time permitted.

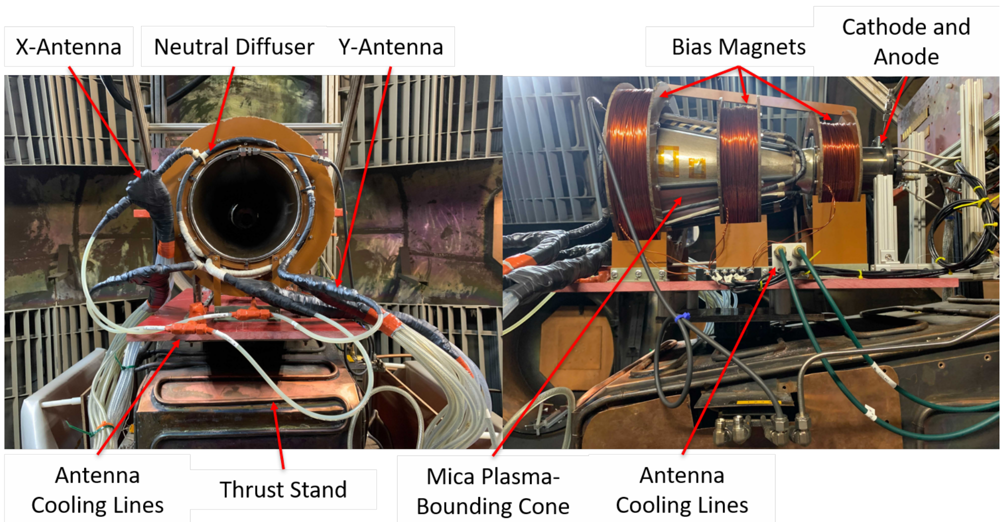

Fig. 9 Close view of the RMFv2 mounted on the thrust stand inside LVTF. Salient features annotated.

C. Thrust stand

One of the major goals of this effort is to perform direct performance measurements of the RMF thruster. This can pose a technical challenge given that most state of the art thrust stands are designed to measure steady-state rather than pulsed devices. However, as was pointed out in Ref. [19], if the pulse rate is sufficiently faster than the natural frequency of a standard pendulum-based thrust stand, it is possible to infer the time-averaged performance. To this end, the RMF thruster was mounted on an inverted pendulum-type thrust stand designed with field-recognized best practices [20] in mind for measuring the performance of Hall thrusters. The thrust stand's natural frequency is approximately 1 Hz, while the RMF thruster was operated at a pulse rate of 75 Hz, with the significantly higher frequency allowing for steady-state thrust measurement.

With that said, as this thrust stand is intended primarily for characterizing steady-state devices, there were a number of technical challenges in adapting its operation to measuring our pulsed device. To illustrate this, we first describe the principle of operation of the system. Figure 10ashows the design of the thrust stand.

When the thruster is switched on, the thrust will apply a force to the thruster mounting plate in the positive x direction as per the coordinate in the figure. This stand is normally operated in null mode, in which current is passed through a magnet known as the null coil applies a force to counteract the thrust, while a separate current is passed through the damper coil to help dampen transients. The current required to maintain zero displacement is calibrated to the thrust using a series of known weights, and the displacement is measured using an optical displacement sensor, labelled ODS in Figure 10aa). An inclinometer meanwhile measures the total inclination of the thrust stand, which is separately calibrated to the force required to maintain null signal. To arrive at the total thrust, the current to the null coil and inclination are both taken into account.

In the RMF case, the electromagnetic interference from the pulsed currents through the antennas made active control impossible by disrupting the control signals. Therefore the stand was operated in a displacement mode, in

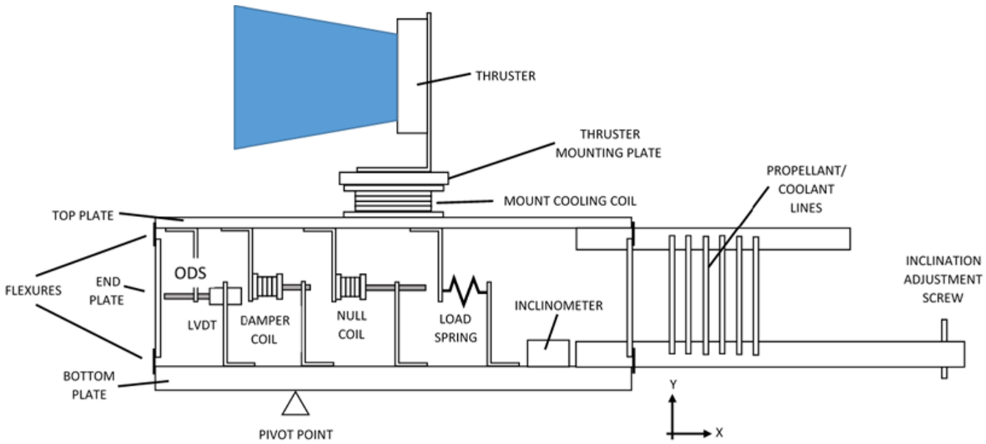

(a)

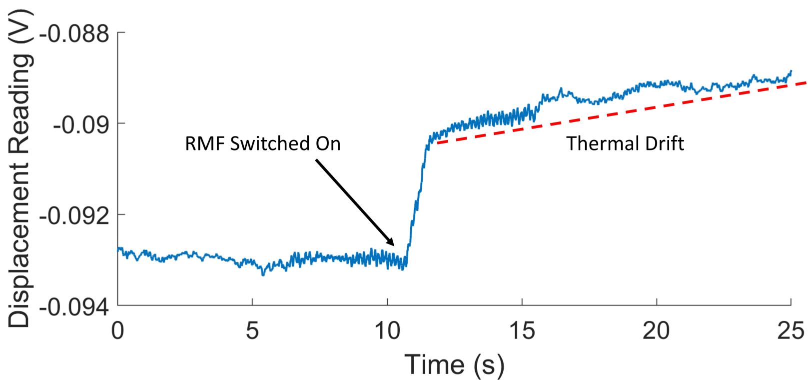

(b)

Fig. 10 a) Schematic of the inverted pendulum thrust stand used b) Example displacement signal produced during a thrust trial.

which displacement and inclination were measured but not controlled.Rather than correlate null coil current to thrust, the displacement itself was calibrated using known weights. Because the displacement is measured using an optical displacement sensor whose transducer is situated outside the vacuum chamber, the displacement measurement itself was unaffected by electrical noise. The inclination, meanwhile, exhibited increased noise, which is reflected in uncertainty in the thrust measurements.

Because the PPU was only capable of running at full power for 5-10 minute intervals due to cooling constraints, it was not possible to operate the thruster at full thermal steady-state. This caused thermal drift to become a concern, so displacement and inclination data were taken immediately before and after the thruster was switched on to eliminate the impact of this drift. An example displacement signal waveform is shown in Figure 10b to illustrate this. Finally, the influence of anomalous thrust due to inductive effects from the current pulse and from line whip to electromagnetic interference on data collection devices must be eliminated. To do so, displacement and inclination waveforms were collected using vacuum shots (no propellant flow), and a correlation was developed to relate the anomalous signal to the amplitude of the current pulse. An anomalous thrust was then determined for each measurement setpoint by using the current amplitude to anomalous thrust correlation, and the false signal was then subtracted.

Other measurement difficulties either limit information gathered or pose as sources of error. Inductance requirements on the cables which carry power to the RMF antennas from the PPU mean the cables must be heavy braided bundles or wide flat strip lines, both of which are difficult to connect to a thrust stand in such a way that stiction is eliminated. As a result, we were able to establish a well-behaved linear calibration curve when adding calibration weights to the stand, but not when removing the weights. This required us to make thrust measurements on thruster activation rather than shut-off, meaning cathode thrust, while anticipated to be quite small, is not included in these measurements. Additionally, while the thrust stand uses a fully optical sensor to measure displacement signal, the inclination, which is also calibrated against, is measured via a transducer mounted inside the stand. Noise introduced on this line due to the RMF pulse required us to perform an additional EMI calibration, which adds another source of error.

V. Analysis Methodology

To extract useful performance data for RMF thruster, several additional steps must be taken beyond raw data collection. In this section, we address the major analyses which we performed to arrive at our results. First we explain the translation of average thrust measurements which include the empty space in the duty cycle to per-pulse measurements. Second, we discuss how to calculate the amount of energy added to the plasma using the antenna current waveform. Third, we establish our early phenomenological efficiency model and define the plume efficiency.

A. Per-pulse versus average performance metrics

Because the repetition rate of 75 Hz and pulse duration of 200 μs combine to yield a total duty cycle of only 1.5%, it is apparent that the thrust measurements taken will be low. However, these 'average' measurements which are read from the thrust stand can be converted to 'per-pulse' measurement, which refer only to the portions of the pulse cycle in which the thruster is truly firing. To this end, the thrust data is taken at the delta between the RMF active and inactive, so that this 'propellant on, but RMF off' condition can be considered as the zero thrust floor. We note that as the cathode does remain on with propellant continuing to flow between pulses, this does not contribute to this thrust measurement.

We consider both thrust and power in this analysis. The momentum generated by a single shot is given by

$$p^* = m^* u_e^*, \tag{30}$$

where the asterisk superscript denotes a per-shot quantity, i.e. p^* is the total momentum from a single shot, m^* is the shot's mass, and u_e^* is its effective exhaust velocity. The actual measured (average) thrust will be given by

$$T_{avg} = \frac{\Delta p}{\Delta t} = p^* f, \tag{31}$$

where Δp is the net impulse over some time period Δt containing many pulses, and f is the shot repetition frequency. With Equations 31 and 30, can arrive at the 'per-pulse' exhaust velocity of

$$u_e^* = \frac{T_{avg}}{m^* f} \tag{32}$$

This formulation requires knowledge of the mass in a given shot. Although propellant remains flowing over the course of a pulse, this is not a large fraction of the actual mass accelerated because the pulse timescale (200 μs) is much shorter than the characteristic fill time of the cone (≈2-3 ms). Therefore, we assume thermal diffusion of the gas throughout the cone has reached steady-state between pulses. Equation 27 has already been derived in this work to determine the number of particles per shot. Multiplying by the mass per particle would then yield the mass per shot due to steady-state thermal diffusion. Including the mass added during the pulse, mass per shot would be given by

$$m^* = \dot{m}\left(\frac{4l}{M\langle c\rangle} + \Delta t_{pulse}\right), \tag{33}$$

although we note that in practice, the mass added during a pulse is found to be small compared to the steady-state mass—less than 5% for this device.

We can apply this process of 'average' to 'per-pulse' conversion to power also to arrive at an per-pulse efficiency measurement. Integrating the total power input to the thruster over a given pulse cycle gives the energy added to the thruster, so that

$$\eta^* = \frac{m^* u_e^{*2}}{2E^*}. \tag{34}$$

The only remaining quantity to be determined is E^*, the energy added to a pulse, which can be found in a similar method to the impulse per pulse by taking $E^* = \frac{P_{avg}}{f}$.

B. Coupling efficiency

We define the coupling efficiency η_c as the fraction of the power injected into the LC resonant circuit which is deposited into the plasma. This metric allows us to separate efficiency losses between the coupling process, which is assumed to be largely a function of the antenna design, and the acceleration process. Antenna current waveforms, such as the one shown in Figure 11, can be used to examine the plasma loading on the circuit. Because the PPU functions by injecting small pulses into a series LC resonator formed by each antenna and its associated tuning capacitor bank, the pulse amplitude is dictated by the real resistance in the circuit and the frequency discrepancy between the natural resonant frequency of the antenna circuit and the frequency of the injected pulses. The presence of plasma serves to increase the effective resistance and reduce the effective inductance of the antenna, thus reducing the amplitude of the current. Antenna current waveforms can be compared between vacuum shots with no plasma present and plasma-loaded shots to determine the amount of energy deposited into the plasma, and therefore the coupling efficiency. What follows is the derivation of this method.

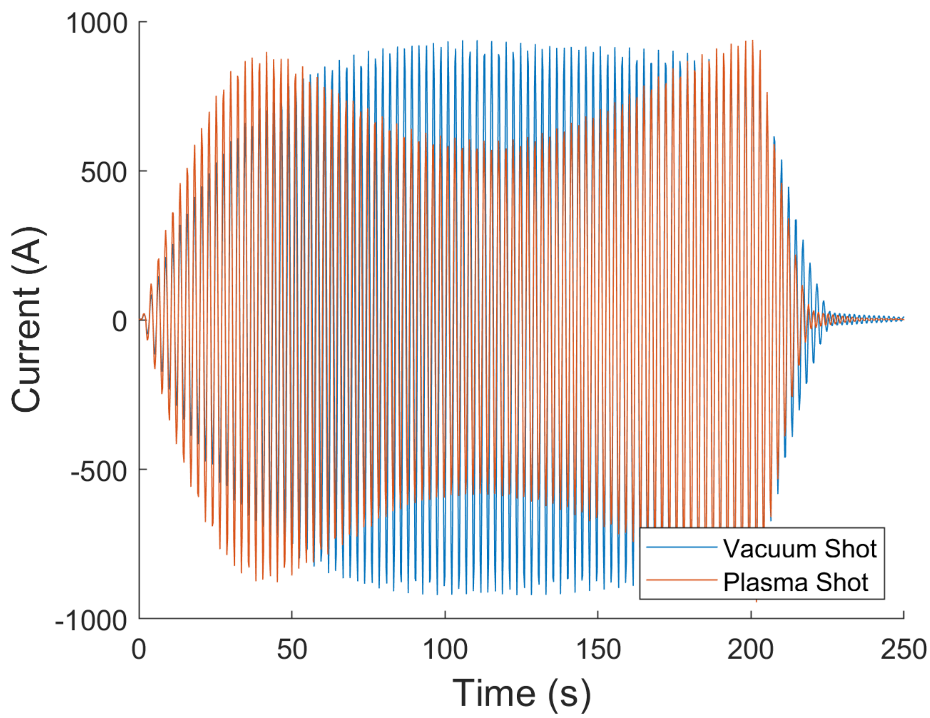

Fig. 11 Example vacuum and antenna current traces for the 1.95 kA peak current setting. The plasma shot is taken at the 45 sccm Xe flow rate, 120 G centerline bias field condition.

For this analysis, V_{DC}, V_{BB}, I_{DC}, I_x, and I_y are as designated in Figure 7. First, we note that electrical power coming through the PPU during a plasma shot can be lost resistively charging the backing capacitor bank, lost resistively while oscillating between the antenna and tuning capacitor bank, or deposited into the plasma. Therefore,

$$\eta_c \equiv \frac{U_p}{U_{LC,p} + U_p}. \tag{35}$$

where U_p is the energy successfully input to the plasma, and U_{LC} is the energy lost due to resistivity while resonating between the antennas and the tuning capacitors. The extra subscript p refers to the fact that this quantity is captured during a shot with plasma present in the thruster, as opposed to a vacuum shot (no plasma), designated by subscript v. We next consider that the total energy input to the PPU by the DC supply during a shot is given by

$$U_{DC,p} = \frac{V_{DC,p} I_{DC,p}}{f}, \tag{36}$$

where we make use of the experimental observation that both $V_{DC,p}$ and $I_{DC,p}$ are flat and can be considered DC values across a pulse or a series of pulses. Meanwhile, the portion of the energy lost while charging the backing capacitor bank is given by

$$U_{R,p} = \frac{\left(V_{DC,p} - V_{BB,p}\right) I_{DC,p}}{f}. \tag{37}$$

This can be substituted into the energy balance, $U_{DC,p} = U_{R,p} + U_{LC,p} + U_p$, to yield an expression for U_p:

$$U_p = \frac{V_{BB,p} I_{DC,p}}{f} - U_{LC,p}.. \tag{38}$$

Like with $V_{DC,p}$ and $I_{DC,p}$, we are able to consider $V_{BB,p}$, which must be measured at the backing capacitor bank, to be a constant DC value at a given operating condition owing to the low-pass nature of the circuit. To fully solve for η_c, we must finally determine $U_{LC,p}$. This is accomplished by firing vacuum shots at the representative DC backing voltage in which there is no plasma present. Energy balance for this situation is given by

$$U_{DC,v} = U_{R,v} + U_{LC,v} \tag{39}$$

$$\Rightarrow U_{LC,v} = U_{DC,v} - U_{R,v} = \frac{V_{BB,v} I_{DC,v}}{f} \tag{40}$$

Separately, we can calculate the energy lost in each individual resonant circuit by integrating the vacuum shot current waveform:

$$\frac{1}{2} U_{LC,v} = R_{LC,x} \int_0^{\Delta t} I_{x,v}^2 dt \approx R_{LC,y} \int_0^{\Delta t} I_{x,y}^2 dt. \tag{41}$$

where R_{LC} is the effective resistance of the LC resonator formed by a given antenna and its tuning capacitor bank, including effects such as switching losses. We have made the assumptions that approximately the same amount of power is deposited into each near-identical antenna, and that the resistance of the LC circuit remains constant throughout the pulse, and between pulses. The second assumption is based on the presence of coolant flowing through both antennas, and the experimental evidence that the temperature of the antennas does not change even over a full 5 minute run time due to this cooling. Substituting Equation 41 into 40, we have the values of the LC resonators' effective resistances:

$$R_{LC,x} = \frac{V_{BB,v} I_{DC,v}}{2f \int_0^{\Delta t} I_{x,v}^2 dt} \tag{42}$$

$$R_{LC,y} = \frac{V_{BB,v} I_{DC,v}}{2f \int_0^{\Delta t} I_{y,v}^2 dt} \tag{43}$$

Now that the resonators' resistances have been determined, which are assumed not to change between a vacuum and plasma shot at similar currents and voltages, we turn back to the plasma shot:

$$U_{LC,p} = U_{LC,p,x} + U_{LC,p,y} = R_{LC,x} \int_0^{\Delta t} I_{x,p}^2 dt + R_{LC,y} \int_0^{\Delta t} I_{x,p}^2 dt \tag{44}$$

$$U_{LC,p} = \frac{V_{BB,v} I_{DC,v}}{2f} \left(\frac{\int_0^{\Delta t} I_{x,p}^2 dt}{\int_0^{\Delta t} I_{x,v}^2 dt} + \frac{\int_0^{\Delta t} I_{y,p}^2 dt}{\int_0^{\Delta t} I_{y,v}^2 dt} \right) \tag{45}$$

Finally, Equations 38 and 45 can be substituted into Equation 35 and rearranged to yield the full analytic result:

$$\eta_c = 1 - \frac{V_{BB,v} I_{DC,v}}{2V_{BB,p} I_{DC,p}} \left(\frac{\int_0^{\Delta t} I_{x,p}^2 dt}{\int_0^{\Delta t} I_{x,v}^2 dt} + \frac{\int_0^{\Delta t} I_{y,p}^2 dt}{\int_0^{\Delta t} I_{y,v}^2 dt} \right) \tag{46}$$

Using Equation 46, we can therefore calculate the coupling efficiency by making measurements of the DC voltage across the backing bank, the DC current sourced from the DC supply, and the antenna current waveform. Because they are effectively constant with time, the backing bank voltage and power supply currents can be made over a long time scale, but the antenna waveform currents must be time-resolved so that integration is possible. First the measurements are made for a series of plasma-loaded shots, then for vacuum shots with similar peak current levels so that the LC resonator's effective resistance is the same between both cases.

C. Plume Efficiency

All other loss mechanisms besides coupling losses are included in what we define as the plume efficiency, η_{pl}, defined as

$$\eta_{pl} = \frac{\eta_T}{\eta_c} \tag{47}$$

$$\eta_{pl}^* = \frac{\eta_T^*}{\eta_c} \tag{48}$$

where η_T is the total efficiency. Note that coupling efficiency is inherently independent of the pulse duty cycle, while the plume efficiency is not. We have left the definition of the plume efficiency so broad due to the relatively limited diagnostics available to us at this time; subsequent work will likely focus on the further development of a more complete phenomenological efficiency model. As it stands, plume efficiency captures such losses as divergence losses, mass utilization, charge utilization, and other such mechanisms.

VI. Results

In this section, we present the results for our performance characterization of the RMF thruster. We first show images of firing. This is followed by a presentation of performance measurements, including those measurements from both thrust stand and antenna current waveforms.

A. Imaging of plume propagation

Figure 12 shows selected frames from high speed video depicting the evolution of RMF shots from the side of the thruster. The frame rate is at 50 kHz, and we depict three operating conditions shots to illustrate the similarities and differences in behavior between setpoints. All cases show the formation of some sort of pulsed plasma ball structure, which develops in the upstream region just outside the mouth of the thrust cone. The plasma structure moves away from the thruster, and in the moderate flow cases appears to detach and continue to move downstream. In the low flow cases, up to 30 sccm, a secondary shot begins to form towards the end of the pulse after the first has been accelerated, as seen in the 200 μs timestamp in Figure 12a). At higher flow rates such as 45 and 60 sccm, no secondary slug can be seen. At the extreme 200 sccm case, no plasma structure detachment occurs, and the plasma has not finished ejection by the end of the pulse.

The formation and detachment of the plasma structure suggests that field reversal is ocuring, in which the magnetic field induced by the RMF is strong enough in magnitude relative to the bias magnetic field to reverse the direction of the overall magnetic field near centerline. This has the effect of creating a plasma structure surrounded by a separatrix. If this is the case, then there are indeed azimuthal currents being driven in the plasma which are interacting with the bias field to produce acceleration.

Figure 13 shows a time-averaged image of the thruster firing. The image was acquired by setting the exposure on a DSLR camera to 10 seconds. Setting the exposure to this length shows distinct structures in the plume. The brightest region appears to be a time-averaged ball of plasma residing near the mouth of the thruster which shows good collimation. Outside it is a weaker region of illumination, likely caused by the expansion of the plasma slugs as they move downstream. Outside all of this is a much weaker region, probably caused by electrons not captured in the plasma structure which remain attached to the bias magnetic field lines.

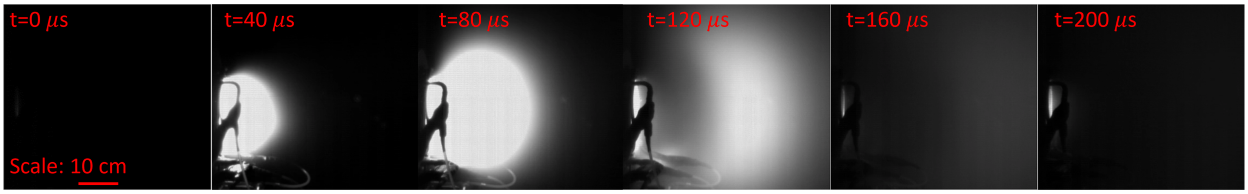

(a)

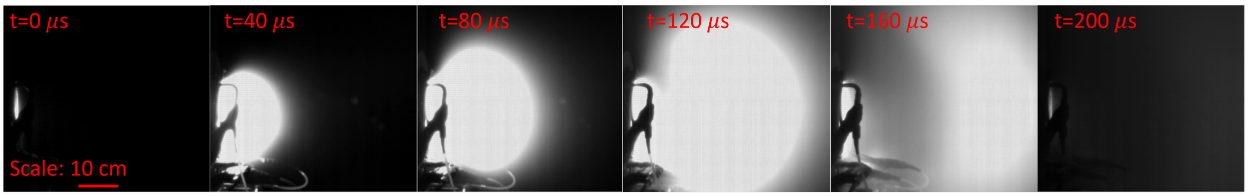

(b)

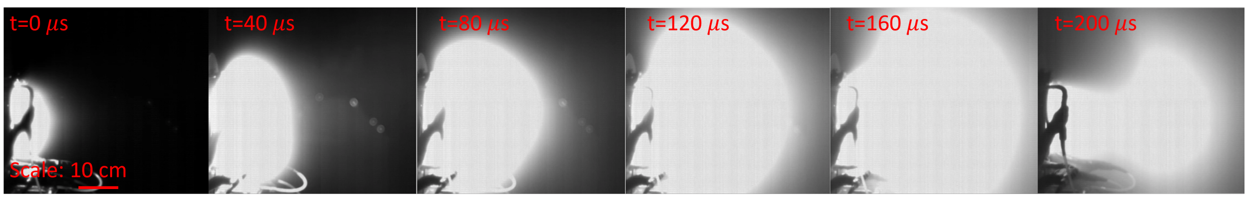

(c)

Fig. 12 High speed video of three representative plasma shots: a) 30 sccm Xe, 80 G Bias, 1.9 kA Antenna current, b) 30 sccm Xe, 80 G Bias, 1.9 kA Antenna current, c) 200 sccm Xe, 120 G Bias, 1.9 kA Antenna current.

B. Current Waveforms

Antenna current waveforms are critical for computing the coupling efficiency as separate from the total efficiency, as discussed in Section V. Figure 11 shows an example vacuum and plasma waveform.

The blue trace, labelled as the Vacuum Shot, was taken with no plasma present. It can be seen to ramp up, then achieve some steady amplitude for the majority of the pulse. This shape is indicative of a series LC circuit being driven at its resonant frequency. In the case of a perfect match between the resonant frequency and the driving frequency, the amplitude is limited only by the real resistance in the circuit. To attempt to match the resonant frequency as best as possible, we employ a tuning procedure before thruster operation. Each antenna is driven at a range of frequencies with a range of phase delays between X and Y antenna driving signals to ensure the maximum equal amplitude on both antennas with a 90° phase delay between the current waveforms. As a result, each antenna is actually driven slightly off its resonance to ensure equal amplitude between the X and Y antennas.

In the plasma-loaded shot, the waveform amplitude can be seen to rise faster than the vacuum shot. The primary reason for this is that, due to the plasma loading on the circuit, we must apply a higher voltage to achieve the same peak current as in the vacuum shot case. Further along in the pulse, the plasma loading becomes more apparent as the waveform takes on a "dogbone" shape. Because the amplitude of the pulse is limited by the difference between the pulse frequency and the resonant frequency of the antennas, the plasma's presence serves to dramatically reduce the current amplitude by changing the effective inductance of the antennas. While plasma is present and highly coupled to the antennas, amplitude is lowered. This can be illustrated by comparing the time steps in Figure 12b) to the waveform in Figure 11, as they are both taken at the same operating conditions. It is seen that in the images where a large plasma discharge is present, the amplitude is less.

Figure 14a) shows the coupling efficiency across all points plotted with respect to flow rate. While there exists a spread in coupling efficiency due to the range of operational parameters investigated, the trend with flow rate is by far the strongest. Recalling the analysis culminating in Equation 29, we should expect that increased flow rate will yield a higher coupling efficiency given a certain energy input and assuming penetration. With a higher energy required for current spin-up, more energy can be added to the plasma before synchronous rotation between the electrons and the

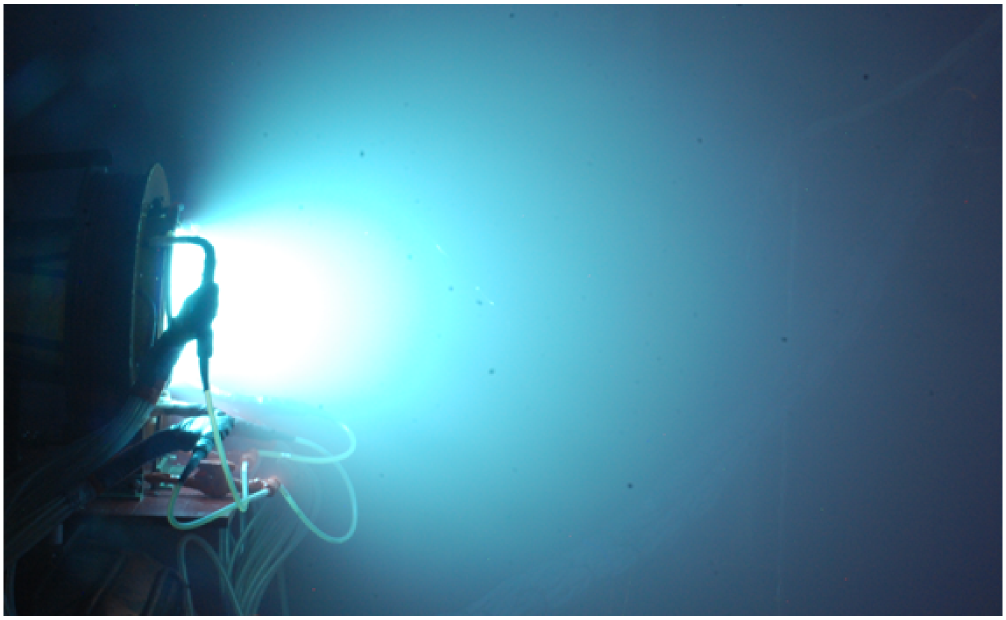

Fig. 13 10 s exposure image of RMFv2 thruster operating at the 45 sccm Xe flow, 1.95 kA peak antenna curent, 120 G centerline bias field condition at 75 Hz repetition rate.

RMF is achieved, leading to reduced loading on the antennas. However, turning to Figure 14b), we find that the specific energy successfully coupled to the plasma appears to be roughly constant with the flow rate. This suggests that the argument that coupling is limited by the maximum spinup energy is likely not true, since such scaling should result in an increasing trend in Figure 14b).

Trends aside, the magnitude of the coupling efficiency peaks at approximately 50% for the conditions investigated. This is significantly higher than the 20% coupling efficiency estimated which was used to guide Figure 8. Such a difference would impact the design by allowing a larger cone size at a given propellant flow rate, since more energy can be available for the propellant. From the perspective of examining paths for future work, we can also be satisfied that we are at least coupling a significant amount of energy to the plasma that the acceleration mechanisms can be studied.

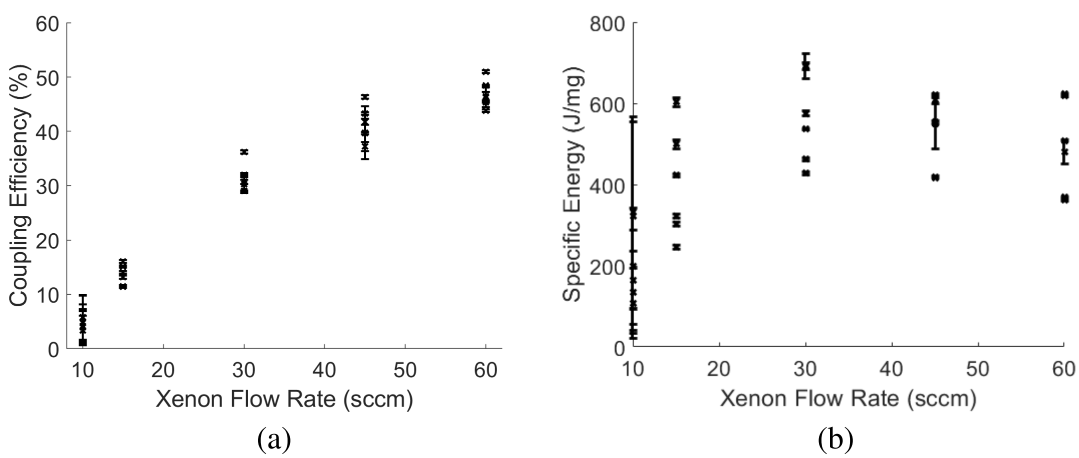

Fig. 14 a)Coupling efficiencies across all measurements, b)Successfully coupled specific energy versus flow rate across all measurements

C. Performance Measurements

For the rest of the data, we turn to thrust stand measurements, beginning with average thrust across the entire duty cycle, as depicted in Figure 15. Keeping in mind that the power levels used to generate these data were between approximately 3 and 4 kW, we recognize that the PEPL RMFv2 does not compete with state of the art electric propulsion at this point. That being said, we wish to highlight that these are the first measurements of their kind to be published to our knowledge. As such, they represent an important step forward in the research of the RMF thruster regardless of absolute performance.

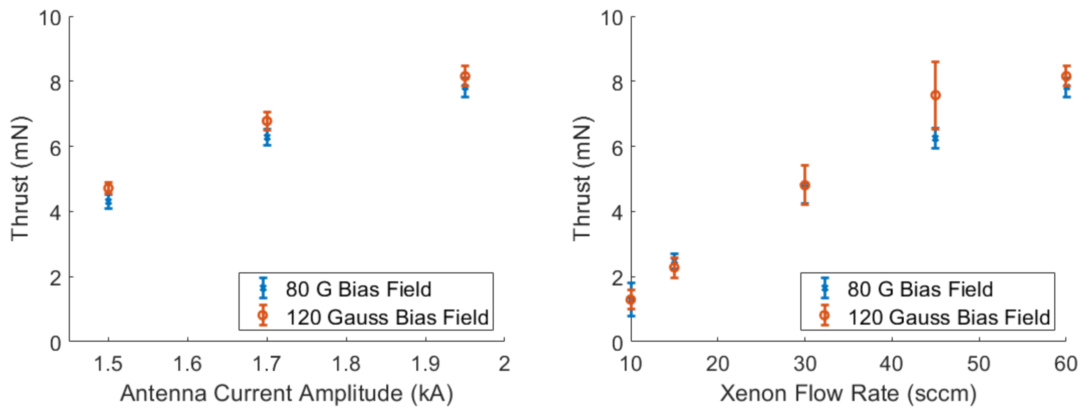

(a) (b)

Fig. 15 Average thrust values (including dead space in the 1.5% duty cycle) as measured from the thrust stand for 200μs pulses at a 75 Hz repetition rate: a)Flow rate fixed at 60 sccm Xe, b) Antenna current fixed at 1.95 kA

We can see several trends in the thrust measurements. First, increasing antenna current amplitude monotonically increases the thrust level from approximately 4.5 mN at the 1.5 kA condition to 8 mN at the full 1.95 kA condition. To first order, the increase in thrust with current is not expected. Indeed, we would expect these trends to be flat since entrainment of electrons only depends on the frequency of the RMF, which is constant (see Sec. II). However, this observed trend suggests that other effects may be at play improving the acceleration process with current. These include improved penetration or improved ionization. We return to a discussion of the physical underpinnings of these trends in Section VII.

The magnetic field has a slight effect of increasing thrust across most flow rates and antenna currents. Equation 8 does suggest that increasing magnetic field should increase thrust, but a much smaller increase is seen than what would be proportional to the increase in field strength. If Equation 8 is indeed correct to describe this device, this would suggest that the self-field term is dominating. However, it is also possible that other undesirable effects such as heating are dominating the acceleration of the plasma over Lorentz force interaction.

These averaged thrust measurements, while useful in that we can identify trends and scaling by comparing tests at the same repetition rate and pulse width, are in some sense artificially low due to the low duty cycle. In practice, a thruster will be operated at much higher repetition rates. However, we can leverage the process discussed in Section V to produce 'per-pulse' measurements of efficiency and specific impulse.

Figure 16 shows the 'per-pulse' plume efficiency trends with both antenna current and flow rate. The maximum magnitude of the plume efficiency increases with antenna current, achieving a maximum value of 1.3%. The distinct upward trend with antenna current amplitude might be attributed to improvements in penetration depth (see Sec. III). In turn, the low value of the maximum achieved efficiency indicates we are not achieving high penetration even at our maximum current. On the other hand, higher current amplitudes are also associated with higher energy per pulse because the backing capacitor bank must be charged to a higher voltage, and thus release more energy per driving pulse, to achieve the higher currents. The increase in energy per pulse could be obscuring the true trend in this case. At a fixed antenna current, increasing flow rate serves to slightly decrease the per-shot plume efficiency, as seen in Figure 16b). This could be related to the specific energy added to the plasma, which would decrease as flow is increased at a field antenna current. Another explanation is reduced penetration as the flow is increased.

Per-pulse specific impulse can also be extracted from the thrust data, which we present in Figure 17, again separated

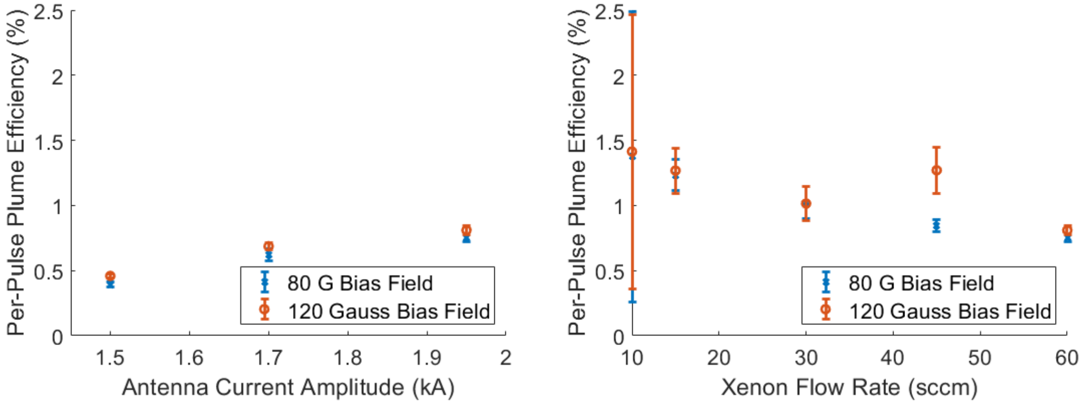

vs flow.png

(a) (b)

Fig. 16 Per-pulse plume efficiencies: a) Flow rate fixed at 45 sccm Xe, b) Antenna current fixed at 1.95 kA

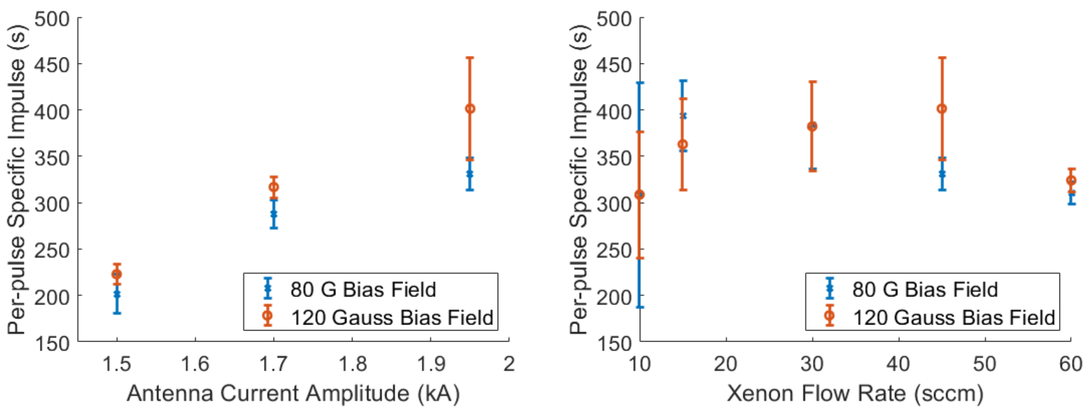

(a) (b)

Fig. 17 'Per-pulse' specific impulse values referring to the per-shot specific impulse rather than a time-averaged value: a) Flow rate fixed at 45 sccm Xe, b) Antenna current fixed at 1.95 kA

between trends with antenna current and flow rate. Per-shot specific impulse can be seen to reach a peak value of approximately 400 s at the 45 sccm, 1.95 kA antenna current, 120 G bias field condition. Figure 17a) shows a clear monotonic increase in specific impulse with antenna current amplitude. This is likely due to the same arguments that contribute to the increased thrust with antenna current at fixed flow. Also similar to thrust trends, we see that the 120 G case yields higher specific impulse than the 80 G case at fixed flow, likely due to the Lorentz force described in Equation 8 increasing with the strength of the bias field, resulting in greater impulse per shot. Trends are less clear with the flow rate, however, although it appears that the specific impulse peaks at a certain flow rate given a fixed antenna current. This could be due to penetration concerns, where full penetration throughout the pulse is not achieved in the 60 sccm, 1.95 kA cases.

Finally, normalizing by the propellant mass per shot, we can compute quantities as functions of the specific energy across all test cases to produce the plots in Figure 18. While ultimately the total efficiency is low, the increasing trend with specific energy gives us optimism for the power scaling capabilities of this device. Indeed, both cases show positive trends, with higher specific energy leading to better performance. This is an important result because it demonstrates in-family behavior with other IPPTs [2], and thus shows that our design is on the right path.

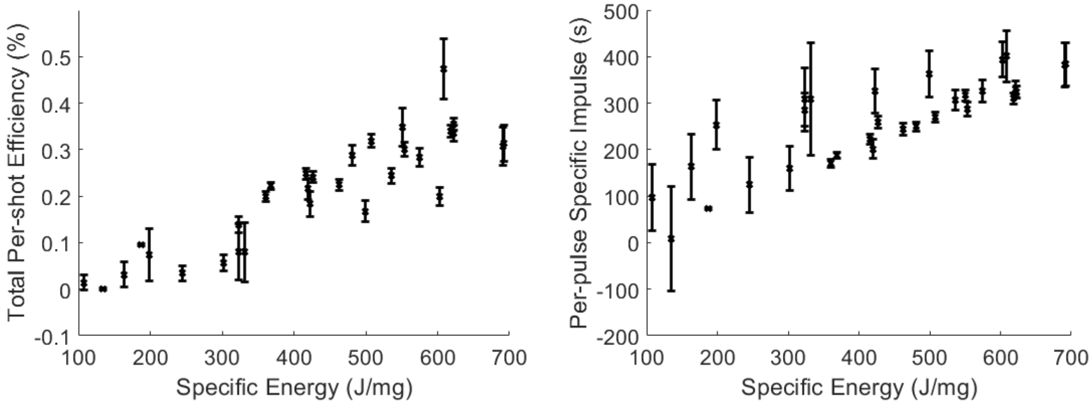

(a) (b)

Fig. 18 Trends with specific energy across all data: a) Total efficiency, b) Specific impulse

VII. Discussion

In this section, we discuss the results in the context of our present understanding of thruster behavior. We first connect the results back to presently understood scaling laws. Second, we discuss how these results could be used to improve thruster performance. Last, we consider the broader implications for the technology moving forward.

A. Relating Trends in Data to Design Scaling Laws

One of the clearest trends seen in the data in Section VI is an increase in performance with antenna current across every measurement. According to the analysis presented in Section II.C, the RMF is well within the penetration regime for every case since a factor of 10 margin was applied to produce Figure 8. Therefore, the positive scaling with antenna current could be simply due to increased energy per pulse being added to the plasma; in the event that current spin-up is not instantaneous, additional energy could be required to achieve synchronous rotation, allowing for deposition of energy beyond the first order estimates. Alternatively, it is possible that increased penetration does indeed play a role here. Examining a typical antenna current waveform such as in Figure 11, we see that the plasma-loaded amplitude is nearly a factor of 2 lower than the nominal pulse amplitude. Considering the relatively loose condition enforced by the inequality of Equation 21, it is reasonable that penetration is lost mid-pulse during the part of the cycle in which it would be most desired, the heavily-loaded middle of the pulse. Further, the penetration condition used to design the thruster assumes a uniform radial density profile which may not be the case in reality and which may make penetration more difficult than expected.

Besides the penetration condition, the other scaling law used to develop the RMFv2's design was the commensurate energy condition, that the inductive energy capable of being stored in the plasma has a limit which depends on the plasma density distribution and the RMF frequency. If this scaling holds, we should observe a maximum specific energy which can be added to the plasma. At first glance, this is supported by the increasing coupling efficiency as more propellant is added to the thruster, as Figure 14a) shows. Equation 29, which describes the scaling which motivates the spinup energy argument, shows that a quadratic scaling between spinup energy and mass flow rate should be expected, and thus a quadratic relationship between the specific energy and the mass flow rate as well. However, the data in Figure 14b) conflicts with this idea, showing roughly constant specific energy as mass flow rate is increased. Therefore, we expect that penetration is likely to be the driving factor behind the increase in coupling efficiency.

Given that both major scaling laws do not seem to be supported by the data, the mechanism of acceleration is called into question. The magnitudes of the specific impulses which Figure 17 shows also serve to call into question the scaling of this device because these low specific impulses are in the regime accessible to a thermal device. Without additional data to verify the azimuthal current drive mechanism is performing successfully, and in light of the disagreement with these putative scaling laws discussed above, we recognize the possibility that we are simply heating the plasma rather than driving acceleration via the Lorentz force. If this is the case, it also explains the relatively weak scaling seen with the bias magnetic field strength, which our scaling laws predict to be more significant.

B. Implications for improving thruster performance

While the performance data gathered is valuable in that they represent the first measurements of their kind, overall performance remains low. By examining the trends presented by the data, we can draw conclusions regarding how to improve thruster performance even before a full performance model is developed and validated.

At the level of analysis afforded us by the data we have, our phenomenological efficiency model splits losses into coupling losses and plume losses, as discussed in Section V, with coupling efficiency peaking around 50% and per-shot plume efficiency peaking at approximately 1.5%. Given the wide gap between these two numbers and the low value of the plume efficiency, immediate research towards improving thruster performance should focus on plume losses. While Figure 16b) does not show clear trends with flow rate, 16a) indicates improvement in plume efficiency with antenna current, and Figure 18a) shows improvement with specific energy. This suggests that we may be operating at antenna currents that are dramatically too low. With these trends, we can conjecture that the penetration condition used to design the RMFv2 is perhaps too lax, especially in light of the reduced antenna current amplitude during the plasma-loaded portion of the pulse.

Unfortunately, exploration of this higher energy regime proves difficult given present PPU limitations. The chief limitation encountered during testing was the power which could be output from the PPU. These upper bounds on output power, which constrain energy per pulse, pulse rate, and total run time, made the collection of reliable data more difficult.

Pulse rate limits made thrust measurement more challenging, as the very low 1.5% duty cycle meant that the actual thrust signal is much smaller than it could be. Increasing the duty cycle to the approximate limits set forth by the assumption of steady-state diffusion throughout the cone would involve a dramatic increase in thrust signal, and therefore more confidence in the results. This would also eliminate the need for the average to per-pulse conversion process, which introduces error due to uncertainty in the true mass of a given plasma shot.

Energy per pulse limits meanwhile constrain our investigation into higher specific powers, which appear to be a promising area of further study based on the upward trends for per-pulse plume efficiency. Attempting to reach those regions of parameter space with the PPU as-is would require dropping the repetition rate more than commensurately due to the nature of the thermal limitations, resulting in even lower duty cycle and further challenges to thrust data resolution.

Challenges aside, further research into the causes of the low plume efficiency is warranted. An understanding of the physics behind why the performance is low could point to solutions besides increase in power level. To gain this understanding, we need more detailed data of the plasma behavior. This will include azimuthal current density levels, which will give information regarding penetration status, electron densities which will tell us if full ionization is being achieved, plasma temperature measurements to determine if power is being wasted heating the gas, and others.

C. Broader Implications for the Technology

The most significant conclusion to be drawn from the results presented above is that the PEPL RMFv2 is indeed functional as a test unit which will allow us to study the acceleration mechanisms further in subsequent tests, and for which we now have a grasp on baseline performance. Additionally, the presence of these results demonstrates that the basic concepts used to produce the thruster's design are valid, or at least on the right track. Throughout Section VI.C we are consistently able to explain trends in the data by referencing the two main criteria used in the thruster's design, RMF penetration and plasma inductive energy storage. Because of the low overall performance relative to state of the art thrusters, it is likely the case that the values used in the RMFv2's design are not optimal, but trends agree with analysis.

The overall low performance of the RMFv2 allows us to conclude additionally that this thruster is not yet competitive with more mature technologies such as Hall thrusters, gridded ion thrusters, or even other (higher TRL) pulsed devices. However, inefficient thruster operation at this point should not lead to the conclusion that the RMF thruster is necessarily an ineffective technology, which owes to the device's relative infancy. At this point, we still lack a validated comprehensive model of RMF thruster operation from which to extract convincing performance upper bounds. It was one of the goals of this work to establish a baseline for guiding development of such a model, which will then allow for such overarching conclusions regarding the technology.

With this in mind, these results constitute the first published nonzero direct measurements of thrust in an RMF thruster that we are aware of, and the existence of a working, freestanding test unit will allow for further investigation of thruster physics. Additionally, the relatively high coupling efficiencies measured show that energy is successfully being transmitted into the plasma. This suggest that the goal of designing an RMF antenna which successfully transfers power to the plasma has been reached, allowing for future research to focus on areas of more acute weakness. The low plume efficiencies measured constitute this weakness, and efforts are warranted to investigate and address the cause.

VIII. Conclusion

In this work, we have sought to fill the need for direct performance measurements of an RMF-driven thruster due to the sparsity of existing data. To that end, we designed and built a new thruster in-house, and made performance measurements. Measurements include 50 kHz high speed video for qualitative observation of the plasma ejection process, antenna current waveform traces to compute coupling efficiency, and thrust stand data. Using these results, we are able to establish several trends which qualitatively confirm our understanding of general operating principles, such as positive performance scaling with specific energy. We also found that energy is successfully being coupled into the plasma but not being efficiently converted from there to directed kinetic energy in the plume. Although performance is low, this work has established a baseline for performance and put forth hypotheses for improvement.

IX. Acknowledgements

This work has been made possible by funding through NSTRF Grant 80NSSC18K1190 and NSTGRO Grant 80NSSC20K1168. Development of the PPU was aided by an SBIR grant in collaboration with Eagle Harbor Technologies.

References

[1] Jahn, R. G., *Physics of Electric Propulsion*, McGraw-Hill Book Company, New York, 1968.

[2] Polzin, K., Martin, A., Little, J., Promislow, C., Jorns, B., and Woods, J., "State-of-the-Art and Advancement Paths for Inductive Pulsed Plasma Thrusters," *Aerospace*, Vol. 7, No. 8, 2020, p. 105.

[3] Anand, M., Crawford, I. A., Balat-Pichelin, M., Abanades, S., Van Westrenen, W., Péraudeau, G., Jaumann, R., and Seboldt, W., "A brief review of chemical and mineralogical resources on the Moon and likely initial in situ resource utilization (ISRU) applications," *Planetary and Space Science*, Vol. 74, No. 1, 2012, pp. 42–48.

[4] Vitug, E., "Lunar Surface Innovation Initiative (LSII)," , Jul 2020. URL `https://www.nasa.gov/directorates/spacetech/game_changing_development/LSII`.

[5] Blevin, H. A., and Thonemann, P. C., "Plasma confinement using an alternating magnetic field," *Nuclear Fusion Supplement, Part 1*, 1962, p. 55.

[6] Slough, J., Kirtley, D., and Weber, T., "Pulsed plasmoid propulsion: The ELF thruster," *31th International Electric Propulsion Conference*, 2009, pp. 20–24.

[7] Weber, T. E., "The Electrodeless Lorentz Force Thruster Experiment," Ph.D. thesis, University of Washington, 2010.

[8] Kirtley, D., Pancotti, A., Slough, J., and Pihl, C., "Steady operation of an FRC thruster on Martian atmosphere and liquid water propellants," *48th AIAA/ASME/SAE/ASEE Joint Propulsion Conference & Exhibit*, 2012, p. 4071.

[9] Furukawa, T., Takizawa, K., Kuwahara, D., and Shinohara, S., "Electrodeless plasma acceleration system using rotating magnetic field method," *AIP Advances*, Vol. 7, No. 11, 2017, p. 115204.

[10] Furukawa, T., Takizawa, K., Yano, K., Kuwahara, D., and Shinohara, S., "Spatial measurement in rotating magnetic field plasma acceleration method by using two-dimensional scanning instrument and thrust stand," *Review of Scientific Instruments*, Vol. 89, No. 4, 2018, p. 043505.

[11] Furukawa, T., Shimura, K., Kuwahara, D., and Shinohara, S., "Verification of azimuthal current generation employing a rotating magnetic field plasma acceleration method in an open magnetic field configuration," *Physics of Plasmas*, Vol. 26, No. 3, 2019, p. 033505.

[12] Sun, Y., Levchenko, I., Lim, J. W. M., Xu, L., Huang, S., Zhang, Z., Thio, F., Potrivitu, G.-C., Rohaizat, M., Cherkun, O., et al., "Miniaturized rotating magnetic field driven plasma system: proof-of-concept experiments," *Plasma Sources Science and Technology*, 2020.

[13] Hugrass, O. T., W N, and Ohnishi, M., "Plasma-circuit Interactions in Rotating Magnetic Field Current Drive," *Plasma Physics and Controlled Fusion*, Vol. 50, February 2008, p. 055008.

[14] Goebel, D. M., and Katz, I., *Fundamentals of Electric Propulsion: Ion and Hall Thruster*, Jet Propulsion Laboratory, California Institute of Technology, 2008.

[15] Myers, C., Edwards, M., Berlinger, B., Brooks, A., and Cohen, S., "Passive Superconducting Flux Conservers For Rotating Magnetic Field Driven Field Reversed Configurations," *Fusion Science and Technology*, Vol. 61, 2012, pp. 86–103.

[16] Sercel, C. L., Woods, J. M., Gill, T., and Jorns, B., "Impact of Flux Conservers on Performance of Inductively Driven Pulsed Plasmoid Thrusters," *AIAA Propulsion and Energy 2020 Forum*, 2020, p. 3632.

[17] Woods, J. M., Sercel, C. L., Gill, T., and Jorns, B., "Performance Measurements of a 60 kW Field-reversed Configuration Thruster," *AIAA Propulsion and Energy 2020 Forum*, 2020, p. 3633.

[18] Viges, E. A., Jorns, B. A., Gallimore, A. D., and Sheehan, J., "University of Michigan's Upgraded Large Vacuum Test Facility," *36th International Electric Propulsion Conference*, 2019.

[19] Wong, A. R., Toftul, A., Polzin, K. A., and Pearson, J. B., "Non-contact thrust stand calibration method for repetitively pulsed electric thrusters," *Review of Scientific Instruments*, Vol. 83, No. 2, 2012, p. 025103.

[20] Polk, J. E., Pancotti, A., Haag, T., King, S., Walker, M., Blakely, J., and Ziemer, J., "Recommended practice for thrust measurement in electric propulsion testing," *Journal of Propulsion and Power*, Vol. 33, No. 3, 2017, pp. 539–555.